

Observation of laser-assisted electron-impact ionization in ultrashort intense laser fields

Takashi Hiroi ^{1,2} Yuya Morimoto ^{3,*} Reika Kanya ^{1,4,5} and Kaoru Yamanouchi ^{1,†}

¹Department of Chemistry, School of Science, The University of Tokyo, 7-3-1 Hongo, Bunkyo-ku, Tokyo 113-0033, Japan

²International Center for Young Scientists, National Institute for Materials Science, 1-2-1 Sengen, Tsukuba, Ibaraki 305-0047, Japan

³Friedrich-Alexander Universität Erlangen-Nürnberg, Staudtstraße 1, 91058 Erlangen, Germany

⁴Department of Chemistry, Faculty of Science, Tokyo Metropolitan University, 1-1 Minami-Osawa, Hachioji-shi, Tokyo 192-0397, Japan

⁵JST PRESTO, 1-1 Minami-Osawa, Hachioji-shi, Tokyo 192-0397, Japan



(Received 17 June 2021; revised 1 November 2021; accepted 2 December 2021; published 21 December 2021)

A laser-assisted ($e, 2e$) [LA($e, 2e$)] process of Ar in an ultrashort (1.2 ps) near-infrared intense laser field, $\text{Ar} + e^- + h\nu \rightarrow \text{Ar}^+ + e^- + e^-$, was observed by coincidence measurements of the fast electron scattered forward within the small-angle range and the slow electron emitted to the wide-angle range. The spectrum of the sum of the kinetic energies of fast and slow electrons exhibited a shoulder structure at the one-photon energy shift from the ($e, 2e$) peak for the Ar $3p$ orbital, which was unambiguously assigned to the LA($e, 2e$) process with the one-photon energy gain. The determined triply differential cross section of the LA($e, 2e$) process with one-photon gain from the laser field was approximately twice as large as a theoretical estimate and this enhancement was regarded as an evidence of the formation of light-dressed states of Ar.

DOI: [10.1103/PhysRevA.104.062812](https://doi.org/10.1103/PhysRevA.104.062812)

I. INTRODUCTION

When atoms and molecules are irradiated with high-energy electrons the kinetic energy of which is larger than the ionization energy of the atoms and molecules, the ionization proceeds during the electron scattering. This phenomenon is called an electron-impact ionization, or an ($e, 2e$) process. If the momentum transfer from the incident electron to the target is sufficiently small in high-energy scattering, the generalized oscillator strength, which is proportional to the cross section of the electron-impact ionization, converges to the optical oscillator strength. Therefore, the optical oscillator strength for the transition to highly excited states of atoms and molecules was determined by the electron-impact ionization before synchrotron radiation facilities became commonly available [1]. When an electron scattered within the solid angle of $d\Omega_a$ and an electron ejected within the solid angle $d\Omega_b$ with the kinetic energy of E_b are detected in coincidence, we are able to determine a triply differential cross section, $d^3\sigma/d\Omega_a d\Omega_b dE_b$, of the ($e, 2e$) processes which carries information on the correlation effects in the electronic wave function of two outgoing electrons [2] as well as on the atomic and molecular orbitals in the momentum space [3].

When an electron is scattered by an atom or molecule in a laser field of an angular frequency ω , the incident electron can gain or lose its kinetic energy by multiples of the photon energy, $n\hbar\omega$, with n being an integer. This phenomenon is called laser-assisted electron scattering (LAES) [4–10]. In a

similar manner, an ($e, 2e$) process assisted by a laser field is called laser-assisted ($e, 2e$) [LA($e, 2e$)] [11]. Mohan and Chand [12] investigated LA($e, 2e$) processes theoretically and showed that the sum of the kinetic energies of the scattered electron and the ejected electron changes by multiples of the photon energy, $n\hbar\omega$, under the presence of a laser field.

If we can detect the scattered electron and the ejected electron produced in the LA($e, 2e$) process induced by an ultrashort-pulsed laser field and determine the triply differential cross sections, we can investigate how and to what extent atomic or molecular orbitals are deformed by the formation of the light-dressed states within the ultrashort time duration because the LA($e, 2e$) process is induced only in the presence of the laser field. However, the signal intensities of LA($e, 2e$) processes in ultrashort (picosecond to femtosecond) pulsed lasers are in general several orders of magnitude smaller than the background ($e, 2e$) signals produced before and after the timing of the irradiation of an ultrashort laser pulse [13].

Höhr *et al.* [14,15] observed an LA($e, 2e$) process of He in a nanosecond high-power laser field ($\lambda = 1064$ nm, $\tau = 7$ ns, 3 J/pulse, $I = 4 \times 10^{12}$ W/cm²) by detecting the ejected electron and He⁺ in coincidence, and found that the triply differential cross section was increased by a factor of 1.2 by the interaction with the light field, but the number of photons, n , involved in the LA($e, 2e$) processes was not identified because the energy resolution was not sufficiently high to resolve the channels with different n values. Because the effect of the formation of light-dressed states appearing on the triply differential cross section varies depending on the number of photons n involved in the LA($e, 2e$) process [16,17], experimental determination of an n -selective cross section of the LA($e, 2e$) process has been highly awaited.

In the present paper, we perform measurements of an ($e, 2e$) process of Ar in an ultrashort near-infrared intense laser field (2×10^{11} W/cm², 1030 nm, 1.2 ps) using an apparatus

*Present address: Ultrashort Electron Beam Science RIKEN Hakubi research team, RIKEN Cluster for Pioneering Research (CPR), RIKEN Center for Advanced Photonics (RAP), 2-1 Hiro-sawa, Wako, Saitama 351-0198, Japan.

†Corresponding author: kaoru@chem.s.u-tokyo.ac.jp

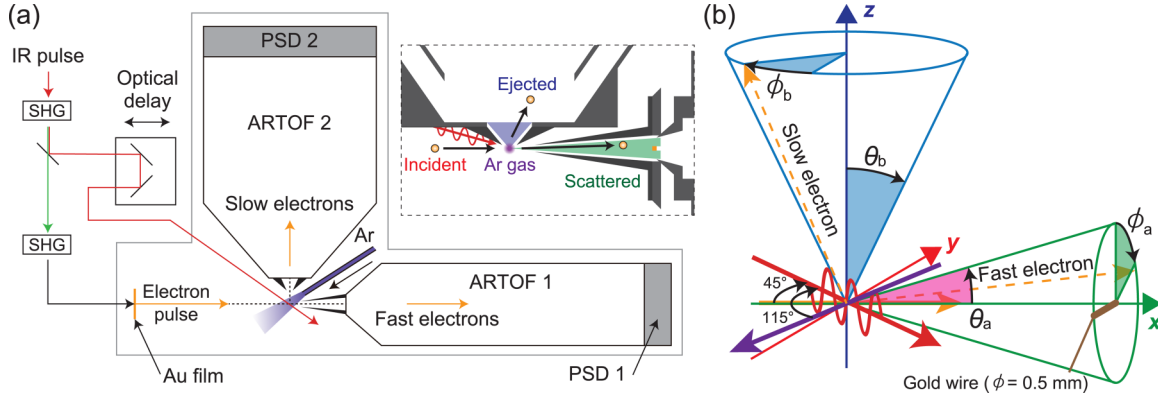


FIG. 1. (a) Schematic of the apparatus for the measurements of $LA(e, 2e)$ processes. SHG, second-harmonic generation; ARTOF, an angle-resolved time-of-flight analyzer; PSD, a position sensitive detector. The inset shows the configuration at the interaction region. A cone-shaped skimmer is attached at the entrance of each analyzer. (b) Definition of the scattering angles and the azimuthal angles for the scattered and the ejected electrons.

with which a scattered electron and an ejected electron from Ar are detected in coincidence, and observe $LA(e, 2e)$ signals unambiguously at the total kinetic energy of the scattered and ejected electrons shifted by one photon energy ($n = +1$). Based on the quantitative evaluation of the triply differential cross section of the recorded $LA(e, 2e)$ signals, we find a firm evidence that the light-dressed state of Ar is formed at the instance of the $(e, 2e)$ process.

II. EXPERIMENT

The measurements of $LA(e, 2e)$ processes of Ar were performed using an apparatus [Fig. 1(a)] consisting of a pulsed electron gun, a scattering chamber, and two sets of angle-resolved time-of-flight (ARTOF) analyzers equipped with a position-sensitive detector (PSD), which are placed in the asymmetric configuration, that is, one analyzer collects the fast electrons scattered forward within the small-angle range while another analyzer collects the slow electrons emitted to the wide-angle range.

The output of a 100-kHz Yb:YAG laser system [1030 nm, 2.5 mJ/pulse, $\tau = 1.2$ ps, linearly polarized—AMPHOS 200 (TRUMPF) pumped by PHAROS 20 (light conversion)] was frequency doubled by a beta barium borate (BBO) crystal. The remaining fundamental pulses were guided to an optical delay stage and were focused on the scattering point (0.6 mJ/pulse, 2×10^{11} W/cm²) so that they crossed an atomic beam of Ar at 115° [Fig. 1(b)]. The frequency-doubled pulses (515 nm, 100 pJ/pulse) were frequency doubled again by another BBO crystal to be converted into fourth-order harmonic generation (FHG) pulses (258 nm, 0.1 pJ/pulse), and the FHG pulses were guided to a photocathode-type electron gun [18,19] by which a pulsed electron beam is generated. The generated electron pulses ($\tau \sim 1$ ps) were accelerated to 1000 eV and were focused on an effusive atomic beam of Ar, which was introduced from a nozzle the orifice diameter of which is 0.5 mm so that the pressure around the detector areas was kept around 1×10^{-4} Pa. The electron pulse, the laser pulse, and the atomic beam cross each other on the same plane. The spatial overlap of the laser pulses and the electron pulses was confirmed by the shadowgraph images of a thin gold

wire (0.1 mm ϕ) placed at the interaction region [18,19]. The polarization of the laser pulses was set to be perpendicular to this plane.

In order to record the $(e, 2e)$ processes by detecting the fast scattered electrons (960–1010 eV) and the slow ejected electrons (<10 eV) in coincidence, we constructed an apparatus equipped with two ARTOF analyzers placed in the asymmetric configuration. One of the two ARTOF analyzers, which is hereafter called the ARTOF analyzer for fast electrons, placed in the direction of the incident electron beam has a small acceptance angle of $\pm 4^\circ$ with the energy resolution of 0.6 eV in the high kinetic-energy range between 960 and 1005 eV. The other ARTOF analyzer, which is hereafter called the ARTOF analyzer for slow electrons, placed just above the interaction region has a large acceptance angle of $\pm 40^\circ$ with the energy resolution of 0.3 eV in the low kinetic-energy range below 10 eV. When the kinetic energy of the incident electrons is 1000 eV, 90% of the scattered electrons can be collected by the ARTOF analyzer for the fast electrons and 10% of the ejected electrons can be collected by the ARTOF analyzer for the slow electrons. By this ARTOF analyzer for the slow electrons, not only the ejected electrons originating from the $(e, 2e)$ process but also the photoelectrons ejected from excited Ar atoms created by the electron-impact excitation processes can be detected. The incident electrons propagating straight without being scattered by the sample gas are blocked by a thin gold wire (0.5 mm ϕ) placed in front of the entrance aperture of the analyzer for the fast electrons. In order to block low-energy secondary electrons originating from the electron impact on the surface of this thin gold wire, we placed cone-shaped skimmers with a small aperture at the entrance of the two ARTOF analyzers.

Both of the analyzers were equipped with a PSD with delay-line anodes (HEX80 and DLD80, RoentDek Handels GmbH), so that the scattering angle and the kinetic energy of the electrons are determined from the position on the detector plane where the electron hits and the time of flight of the electrons. The signals detected by each PSD were amplified by an amplifier (FAMP8, RoentDek Handels GmbH), processed by a constant fraction discriminator (CFD7x and CFD8c, RoentDek Handels GmbH), and converted into digital data

by a time-to-digital convertor (TDC8HPi, RoentDek Handels GmbH). After the synchronization of the digital data from the two ARTOF analyzers, a scattered electron and an ejected electron originating from the same ($e, 2e$) event are detected in coincidence.

In order to obtain the laser-assisted signals and the field-free signals under the same experimental conditions, we measured the ($e, 2e$) processes at three different delay times of the electron pulse with respect to the laser pulse: $\Delta t = 0$ for the laser-assisted signals, $\Delta t = -67$ ps (the electron pulse first), and $\Delta t = +67$ ps (the laser pulse first) for the field-free signals. In the present paper, a reduction of the background signals is crucial because the signal intensity of the LA($e, 2e$) process with a one-photon energy shift under the present experimental conditions is weaker than the signal intensity of the field-free ($e, 2e$) process by a factor of 10^3 . By reducing the number of electrons per electron pulse as low as around 10, we confirmed that the false coincidence events did not interfere with the detection of LA($e, 2e$) events. Because of the high collection efficiency of the apparatus, we are able to record the ($e, 2e$) event of Ar with the count rate of 1 count/s even though the averaged electron current (10^6 electrons / 1 s ~ 0.1 pA) is several orders of magnitude lower than that in the conventional coincidence experiment (≈ 1 μ A).

III. RESULTS AND DISCUSSION

A. Energy correlation map for the fast electrons and the slow electrons

Before examining the recorded LA($e, 2e$) signals in Sec. III C, we first confirm in this subsection that the energy resolution of the coincidence measurement of the fast scattered electrons and the slow ejected electrons is sufficiently high and, then, confirm in the next subsection (Sec. III B) that the laser-assisted processes are induced by the irradiation of the ultrashort laser pulses.

The energy correlation maps between the fast electrons (the scattered electrons) and the slow electrons (the electrons ejected from Ar), which were detected in coincidence, are shown in Fig. 2 at the three different delay times of the incident electron pulse with respect to the laser pulse. The data accumulation time was 20 h at $\Delta t = 0$, and 10 h at delay times of $\Delta t = -67$ and $+67$ ps. The horizontal axis represents the kinetic energy of the fast electrons, E_{fast} ; the corresponding electron energy loss, $E_{\text{loss}} = 1000 \text{ eV} - E_{\text{fast}}$, is shown by the upper scale; and the vertical axis represents the kinetic energy of the slow electrons, E_{slow} . When the sample gas was irradiated with the laser pulse first, then, with the electron pulse at $\Delta t = 67$ ps, only a straight-line structure with the slope of -1 was observed as shown in Fig. 2(a), which can be assigned to the field-free electron-impact ionization of Ar, in which one of the outermost $3p$ electrons is ejected.

As shown in Fig. 2(c), when the sample gas was irradiated with the electron pulse first, then, with the laser pulse at $\Delta t = -67$ ps, several spots were observed in the kinetic-energy range of $E_{\text{slow}} < 1$ eV and $E_{\text{fast}} > 984.2$ eV ($E_{\text{loss}} < 15.8$ eV) in addition to a straight-line structure with the slope of -1 . Because the energy losses of the fast electrons at these spots are smaller than the ionization potential of Ar (15.8 eV),

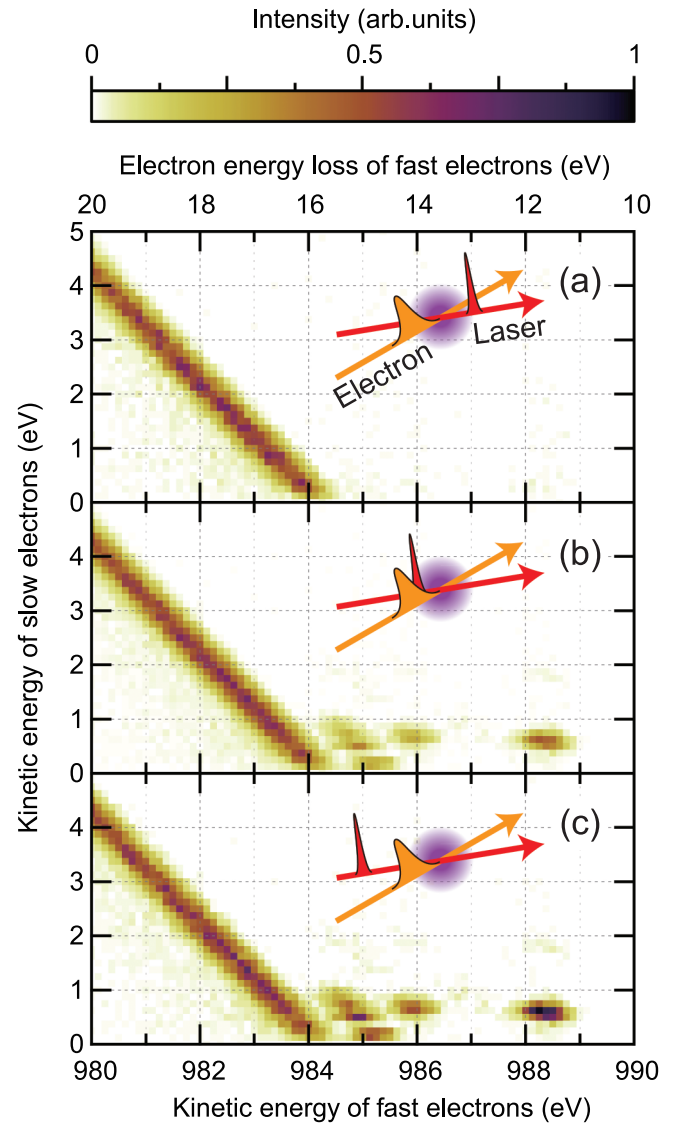
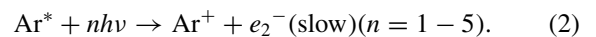
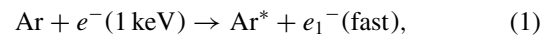


FIG. 2. Energy correlation maps for the fast electrons and the slow electrons generated by the electron-impact excitation of Ar in the ultrashort-pulsed laser field at the delay times of (a) $\Delta t = +67$ ps, (b) 0 ps, and (c) -67 ps. The signal intensities in these three maps are normalized by the respective accumulation times.

they are assigned to the electron-impact excitation processes followed by the photoionization of the resultant electronically excited Ar^* represented as



The assignments of the respective spots are shown in Fig. 3 and Table I. In addition to the electron-impact excitations to $\text{Ar } 3p^5ns^1$ and $\text{Ar } 3p^5nd^1$, which are optically allowed processes, the excitation to $\text{Ar } 3p^54p^1$, which is an optically forbidden process, and the above-threshold ionization processes from $\text{Ar } 3p^5ns^1$ and $\text{Ar } 3p^5nd^1$ are also identified.

The sum of the kinetic energy (E_{fast}) of the fast electron produced in Eq. (1) and the kinetic energy (E_{slow}) of the slow

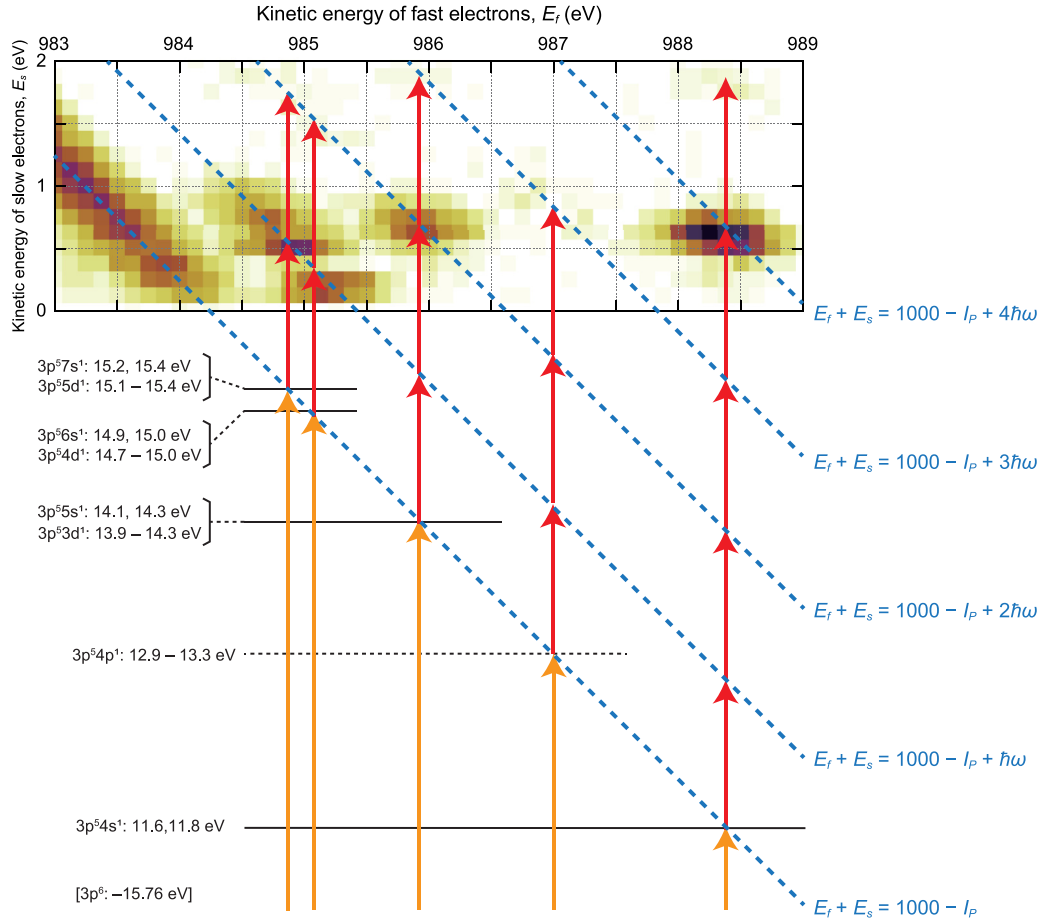


FIG. 3. Assignments of the peak profiles appearing in the energy correlation map for the fast and slow electrons generated by the electron-impact excitation of Ar in the ultrashort (1.2 ps) laser field at $\Delta t = -67$ ps. The ionization potential of Ar (15.76 eV) is denoted as I_p .

electron produced in Eq. (2) can be expressed as

$$E_{\text{fast}} + E_{\text{slow}} = 1000 \text{ eV} - I_p + n \times 1.2 \text{ eV}, \quad (3)$$

where I_p stands for the ionization potential. The lines given by Eq. (3) with the different photon numbers are drawn by broken lines in Fig. 3. In order to eliminate the contribution from the signal originating from Eqs. (1) and (2), only the fast electrons the energy loss of which is larger than 16 eV, which is larger than the ionization potential of Ar (15.76 eV), were used for the analysis for LA(e , 2 e) processes.

Because the yield of the photoelectrons from Ar* generated via Eq. (2) is sensitive to the delay time Δt , the photoelectron yield is used for the determination of the zero delay time ($\Delta t = 0$) at which the photoelectron yield becomes a half of that obtained when the electron pulse comes prior to the laser pulse with no temporal overlap ($\Delta t < -50$ ps). The energy correlation map obtained at $\Delta t = 0$ is shown in Fig. 2(b).

The energy resolutions of the analyzers for the fast and slow electrons are estimated to be 0.6 and 0.3 eV, respectively, from the horizontal and vertical full width at half maximum (FWHM) widths of the spot located at 988.4 eV for the fast

TABLE I. Assignments of the peak profiles in Fig. 3 to the electron-impact excitation processes of Ar.

$E_{\text{fast}} / \text{eV}$	$E_{\text{slow}} / \text{eV}$	n	Assignment of Ar*	Comment
988.0–988.6	0.5–0.8	4	$3p^5 4s^1$	ATI
	1.7–1.9	5		
986.7–987.3	0.6–1.0	3	$3p^5 4p^1$	Nondipole excitation
985.7–986.1	0.6–0.8	2	$3p^5 3d^1, 3p^5 5s^1$	ATI
	1.7–2.0	3		
985.0–985.4	0.0–0.3	1	$3p^5 4d^1, 3p^5 6s^1$	ATI
	1.3–1.5	2		
984.6–985.2	0.4–0.6	1	$3p^5 5d^1, 3p^5 7s^1$	ATI
	1.6–1.9	2		

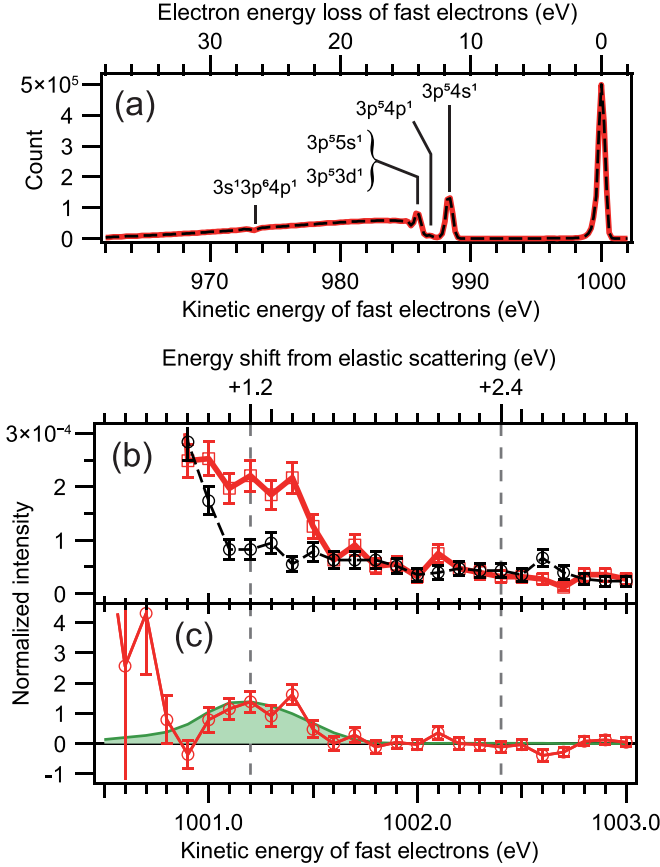


FIG. 4. (a) The energy spectra of scattered electrons obtained by integrating the signals over the scattering angle range of $<4^\circ$ without considering the coincidence detections with the ejected electrons. Red solid line, electron signals with the laser field; black broken line, background signals. (b) The enlarged view of panel (a) in the energy region of 1000.5–1003.0 eV. The error bars are estimated from the square roots of the signal counts. (c) Red circles, the signals with the laser field after the subtraction of the backgrounds; green solid curve with the filled area underneath, the LAES ($n = +1$) spectrum calculated based on the Kroll-Watson theory. The vertical axes for panels (b) and (c) are normalized by the elastic-scattering signals.

electrons and 0.6 eV for the slow electrons in Fig. 3, which is assigned as an electron-impact excitation to $\text{Ar}^*(3p^5 4s^1)$ followed by the four-photon ionization. From these resolutions, the energy resolution of the sum of the kinetic energies of fast and slow electrons was estimated to be $\sqrt{0.6^2 + 0.3^2} = 0.7$ eV, which is sufficiently high to resolve the one-photon energy shift (1.2 eV) induced by the laser-assisted processes.

B. Laser-assisted electron scattering

Figure 4(a) shows the energy spectra of the fast electrons obtained by integrating the observed electron signals over the scattering angle range of $<4^\circ$. The red solid line shows the energy spectrum of the electrons scattered in the laser field ($\Delta t = 0$). The black broken line shows the energy spectrum of the background electrons scattered under no laser field conditions obtained as the sum of the energy spectra recorded at $\Delta t = -67$ and $+67$ ps, both of which were confirmed to overlap almost completely with each other.

In both of the energy spectra, in addition to the peak assigned to the elastic electron scattering ($E_{\text{loss}} = 0$ eV), the peak profiles assigned to the inelastic electron scattering can be identified, which are accompanied by the electronic excitation of Ar to $3p^5 4s^1$ ($E_{\text{loss}} = 11.62$ and 11.83 eV), $3p^5 4p^1$ ($E_{\text{loss}} = 12.91$ – 13.33 eV), $3p^5 5s^1$ ($E_{\text{loss}} = 14.09$ and 14.26 eV), and $3p^5 3d^1$ ($E_{\text{loss}} = 14.15$ and 14.30 eV) [20]. The dip structure appearing at 973.4 eV is assigned to the excitation of Ar to the autoionizing resonance ($3s^1 3p^6 4p^1$) located at $E_{\text{loss}} = 26.62$ eV [21].

Figure 4(b) shows the enlarged view of the energy spectrum at $\Delta t = 0$ and the sum of the energy spectra at $\Delta t = -67$ and $+67$ ps in the energy region of 1000.5–1003.0 eV, in which the vertical axis is scaled so that the intensity of the elastic signals becomes unity. As shown in Fig. 4(b), when the laser pulse overlaps temporally with the electron pulse, the signal intensity increases at the kinetic-energy shift of 1.2 eV measured from the strong peak of the elastic scattering. This peak appearing at the energy shift of 1.2 eV can be assigned to LAES for $n = +1$. In Fig. 4(c), the LAES signals represented by red open circles are extracted by the subtraction of the background spectrum [black open circles in Fig. 4(b)] from the energy spectrum of the electrons scattered in the laser field [red open squares in Fig. 4(b)].

The relative intensities of the LAES signals were calculated numerically using the Kroll-Watson formula [22]. The differential cross section for the n -photon LAES process is given in atomic units as

$$\frac{d\sigma_n}{d\Omega} = \frac{|\mathbf{k}_{f,n}|}{|\mathbf{k}_i|} J_n^2(\xi_{\text{LAES}}) \frac{d\sigma_{\text{el}}}{d\Omega}, \quad (4)$$

$$\xi_{\text{LAES}} = \frac{E_0}{\omega^2} \cdot (\mathbf{k}_i - \mathbf{k}_{f,n}), \quad (5)$$

where \mathbf{k}_i is the wave vector of an incident electron and $\mathbf{k}_{f,n}$ is the wave vector of a scattered electron, J_n is the n th-order Bessel function of the first kind, \mathbf{E}_0 is an electric-field vector of the laser field, and $\frac{d\sigma_{\text{el}}}{d\Omega}$ is a differential cross section of the field-free elastic scattering.

In order to simulate the n -photon LAES intensity, $I_n(\theta_a, \phi_a)$, we have to consider that the scattered electron intensity is proportional to the intensity of the elastic scattering under the field-free conditions $I_0(\theta_a, \phi_a)$, the gas density $\rho_g(\mathbf{r})$, and the electron density of the electron pulse $\rho_e(\mathbf{r}, t)$. In addition, ξ_{LAES} depends on the electric-field vector of the laser field, $\mathbf{E}_0(\mathbf{r}, t)$. In order to take account of the \mathbf{r} and t dependences of the gas beam, the electron pulse, and the laser pulse, we performed the spatiotemporal integration for discrete values of θ_a and ϕ_a as

$$\begin{aligned} I_n(\theta_a, \phi_a) &\propto \int_{x_{\min}}^{x_{\max}} dx \int_{y_{\min}}^{y_{\max}} dy \int_{z_{\min}}^{z_{\max}} dz \int_{t_{\min}}^{t_{\max}} dt \\ &\times \frac{|\mathbf{k}_{f,n}(\theta_a, \phi_a)|}{|\mathbf{k}_i|} J_n^2 \left\{ \frac{E_0(\mathbf{r}, t)}{\omega^2} \cdot [\mathbf{k}_i - \mathbf{k}_{f,n}(\theta_a, \phi_a)] \right\} \\ &\times \rho_g(\mathbf{r}) \rho_e(\mathbf{r}, t) I_0(\theta_a, \phi_a). \end{aligned} \quad (6)$$

In our experimental configuration, the forms of $\rho_g(\mathbf{r})$, $\rho_e(\mathbf{r}, t)$, and $\mathbf{E}_0(\mathbf{r}, t)$ are expressed as

$$\rho_g(\mathbf{r}) = N_g \exp\left[-\frac{(y \cos 70^\circ - x \sin 70^\circ)^2}{2\sigma_{gH}^2}\right] \exp\left[-\frac{z^2}{2\sigma_{gV}^2}\right], \quad (7)$$

$$\rho_e(\mathbf{r}, t) = N_e \exp\left[-\frac{(x - v_e t)^2}{2\sigma_{ex}^2}\right] \exp\left[-\frac{y^2}{2\sigma_{ey}^2}\right] \exp\left[-\frac{z^2}{2\sigma_{ez}^2}\right], \quad (8)$$

$$\mathbf{E}_0(\mathbf{r}, t) = \mathbf{E}_{\text{peak}} \exp\left[-\frac{(x \cos 45^\circ + y \sin 45^\circ - ct)^2}{2\sigma_{l, x+y}^2}\right] \\ \times \exp\left[-\frac{(y \cos 45^\circ - x \sin 45^\circ)^2}{2\sigma_{l, x-y}^2}\right] \exp\left[-\frac{z^2}{2\sigma_{lz}^2}\right], \quad (9)$$

where N_g and N_e are the normalization factors, and \mathbf{E}_{peak} is an electric field at the peak position. We assumed that the spatial distributions of the gas beam, the electron pulse, and the laser pulse are expressed by Gaussian shapes, $\exp(-X^2/2\sigma^2)$. The FWHMs of the Gaussian functions, $2\sqrt{2 \ln 2} \sigma$, are determined experimentally as $\sigma_{gH} = \sigma_{gV} = 2.0$ mm for the gas beam, $\sigma_{ey} = \sigma_{ez} = 0.6$ mm and $\sigma_{ex} = 23 \mu\text{m}$ (1.2 ps) for the electron pulses, and $\sigma_{l, x-y} = 0.5$ mm, $\sigma_{lz} = 0.4$ mm, and $\sigma_{l, x+y} = 0.36$ mm (1.2 ps) for the laser pulses.

The integrals of Eq. (6) are evaluated numerically at given sets of discrete numerical values of (θ_a, ϕ_a) . For the scattering angle θ_a , nine values in the range between 0° and 4° at an interval of 0.5° are adopted, and, for the azimuthal angle ϕ_a , 12 values in the range of 360° at an interval of 30° are adopted. Because $I_n(\theta_a, \phi_a)$ is expressed using the experimentally obtained $I_0(\theta_a, \phi_a)$ as shown in Eq. (6), the effect of the inhomogeneity in the position dependence of the detector sensitivity and the existence of a thin shadow area where the scattered electrons are blocked by the gold wire ($\phi_a \sim 270^\circ$) are automatically compensated in the simulation. The result of the simulation plotted in Fig. 4(c) with a solid smooth curve is in good agreement with the observed intensity profile quantitatively [23].

The red filled circles in Figs. 5(a) and 5(b) show the singly differential cross sections of the LAES process as a function of the scattering angle, θ_a , and the azimuthal angle, ϕ_a , respectively, calculated by the observed two-dimensional (2D) map of the scattering signals in the energy range of 1001.0–1001.5 eV. The simulated signal intensities calculated using the Kroll-Watson theory connected by the black broken line are in good agreement with the observed cross sections connected by the red solid line. The azimuthal angle dependence of the LAES signal in Fig. 5(b) shows a squared cosine shape, which is consistent with the polarization dependence of the cross section of the LAES signals. The decrease in $d\sigma/d\phi_a$ around $\phi_a \sim 270^\circ$ is ascribed to the shadow of the gold wire that blocks the scattered electrons.

C. Laser-assisted ($e, 2e$)

For the respective ($e, 2e$) events recorded in coincidence, the sum of the kinetic energies for the fast and slow electrons

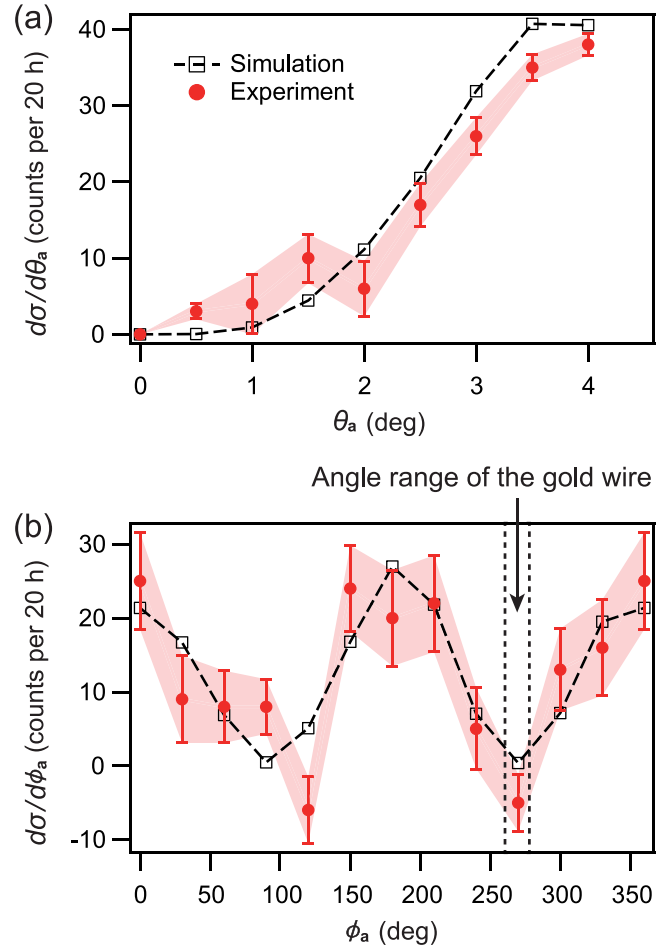


FIG. 5. Red filled circle, the observed singly differential cross sections for the laser-assisted elastic electron scattering: (a) $d\sigma/d\theta_a$ and (b) $d\sigma/d\phi_a$. The error bars are connected so that the uncertainties are shown with the shaded area. Black broken lines, calculated singly differential cross sections obtained using the Kroll-Watson theory.

is determined. The yield of the ($e, 2e$) processes obtained by integrating the signals over the detection angle ranges is plotted as a function of the sum of the kinetic energies as shown in Fig. 6(a), which is hereafter called the sum-energy spectrum. The red solid line shows the sum-energy spectrum for the data obtained at $\Delta t = 0$, and the black broken line shows the sum-energy spectrum obtained as the sum of the sum-energy spectra recorded at $\Delta t = -67$ and $+67$ ps, corresponding to the background spectra, both of which were found to overlap almost completely with each other. Two peaks appearing at 984.2 and 970.8 eV correspond to the electron-impact ionization from the Ar $3p$ (15.76 and 15.94 eV) and $3s$ (29.24 eV) orbitals, respectively. The peak intensity for the Ar $3s$ orbital at 29.24 eV is one order of magnitude smaller than that for the Ar $3p$ orbitals at 15.76 and 15.94 eV, which is consistent with the theoretical cross sections of the electron-impact ionization of the Ar $3p$ and $3s$ orbitals [25]. The weak tail structure of the Ar $3p$ peak extending towards the lower kinetic-energy side from 983.5 eV is assigned to the electron-impact ionization from the Ar $3p$ orbital in which the fast scattered electron

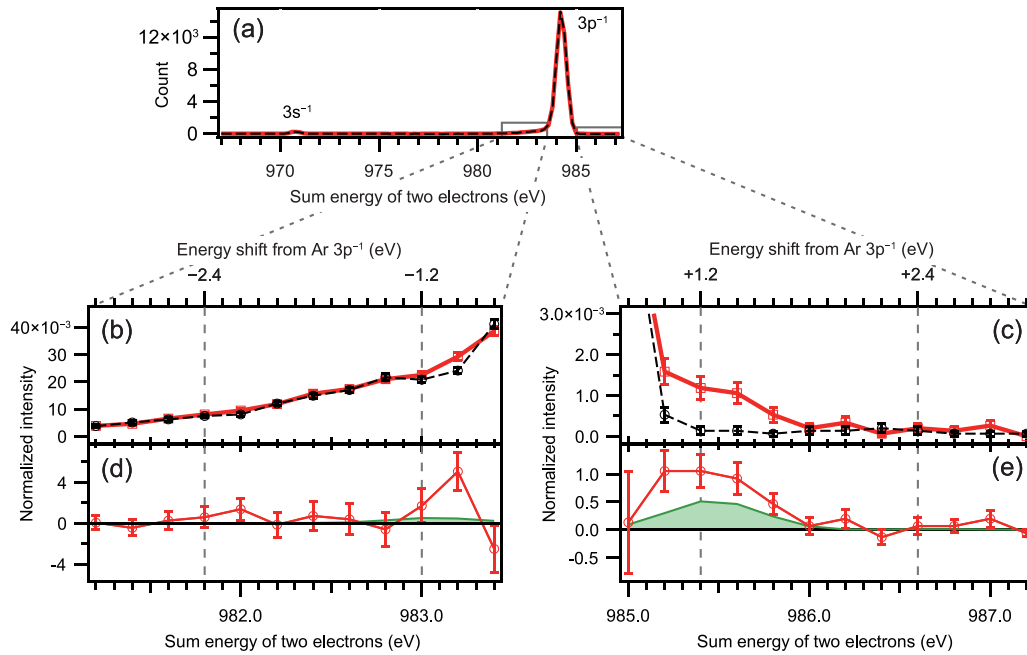


FIG. 6. (a) The sum-energy spectra of the scattered and ejected electrons obtained by integrating the signals over the detection angle ranges. Red solid line, electron signals with the laser field; black broken line, background signals. (b), (c) The enlarged view of the energy region of 981.2–983.4 and 985.0–987.2 eV, which are surrounded by the rectangle in panel (a). (d), (e) The LA($e, 2e$) spectra in the energy region of panels (b) and (c). Red circles, the difference spectrum obtained by the subtraction of the backgrounds from the signals with the laser field; green solid line with the filled area underneath, the calculated LA($e, 2e$) ($n = -1$ and $+1$) spectrum based on the theory proposed by Cavaliere *et al.* [24]. The vertical axes for panels (b)–(e) are normalized by the ($e, 2e$) signals of Ar $3p^{-1}$.

is scattered again elastically by the residual Ar gas in the ARTOF apparatus, resulting in the longer flight time.

Figures 6(b) and 6(c) show the enlarged views in the energy region of 981.2–983.4 and 985.0–987.2 eV, respectively. The scale of the vertical axis is normalized with respect to the intensity of the ($e, 2e$) peak for the Ar $3p$ orbital shown in Fig. 6(a). It can be seen in Fig. 6(c) that a shoulder structure shows up in the signal intensity at 985.4 eV, that is, the kinetic energy shifted by 1.2 eV from the ($e, 2e$) peak for the Ar $3p$ orbital. This shoulder structure appearing in the ($e, 2e$) signals can be assigned to the LA($e, 2e$) process with $n = +1$. By the subtraction of the sum-energy spectrum of the background signals [black open circles in Figs. 6(b) and 6(c)] from the sum-energy spectrum recorded with the laser field [red open squares in Figs. 6(b) and 6(c)], the LA($e, 2e$) spectrum is obtained as shown in Figs. 6(d) and 6(e).

On the other hand, the LA($e, 2e$) process of the Ar $3p$ orbital with $n = -1$ is expected to appear at the sum-energy of 983.0 eV with the same signal intensity as $n = +1$. As shown in the enlarged view in the energy region of 981.2–983.4 eV, where the tail structure extends towards the lower-energy side, the sum-energy spectrum recorded with the laser field [red open squares in Fig. 6(b)] exhibits a small amount of increase at the energy shift of around -1.0 eV compared with the background spectrum [black open circles in Fig. 6(b)]. It is possible that this signal increase is assigned to the LA($e, 2e$) process of the Ar $3p$ orbital with $n = -1$. Considering that the intensity of the Ar $3s$ peak is only 2×10^{-2} of the Ar $3p$ peak as shown in Fig. 6(a), we can predict that the

signal intensity of the LA($e, 2e$) process of the Ar $3s$ orbital is 2×10^{-5} of the Ar $3p$ peak at 984.2 eV, which is even smaller than the noise level of the sum energy spectrum of the order of 10^{-3} – 10^{-4} . Therefore, we expect that the signals of the LA($e, 2e$) process of the Ar $3s$ orbital with $n = +1$ and -1 are buried in the noise of the spectrum. Indeed, we were not able to recognize any peaks assignable to the LA($e, 2e$) process of the Ar $3s$ orbital with $n = +1$ and -1 in the sum energy spectrum shown in Fig. 6(a).

The relative intensities of the LA($e, 2e$) signals under the present experimental conditions were estimated numerically using the formula for the triply differential cross section of a LA($e, 2e$) process derived by Cavaliere *et al.* [24], in which the scattering electron-light interaction was treated explicitly using Volkov wave functions for the incoming and the outgoing electrons and the electron-atom interaction was treated by the first Born approximation, while the atom-light interaction was neglected. The final state of the atom is expressed as a continuum wave function with a slow ejected electron having the asymptotic momentum k_b , modulated by the laser field based on the ansatz proposed by Jain and Tzoar [26]. A numerical factor that compensates the flux changes originating from the energy gain or loss is approximated to be 1 because the photon energy (1.2 eV) is sufficiently smaller than the incident electron energy (1000 eV), and, consequently, the flux change originating from the photon exchange is of the order of 0.1%, which is negligibly small. Under this approximation, the triply differential cross section for the LA($e, 2e$) n -photon absorption ($n > 0$) or emission ($n < 0$) process in atomic units, $d^3\sigma_n/d\Omega_a d\Omega_b dE_b$, is

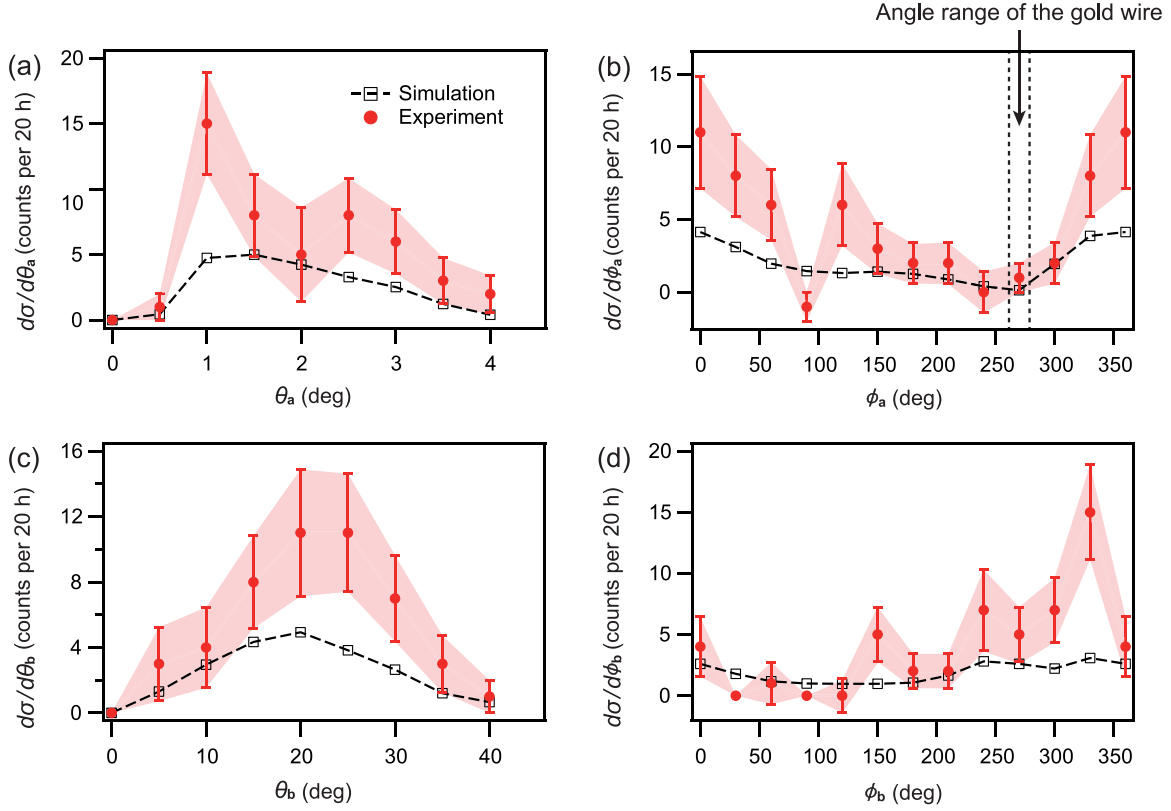


FIG. 7. Red filled circle, observed singly differential cross sections for the laser-assisted ($e, 2e$) processes: (a) $d\sigma/d\theta_a$, (b) $d\sigma/d\phi_a$, (c) $d\sigma/d\theta_b$, and (d) $d\sigma/d\phi_b$. The error bars are connected so that the uncertainties are shown with the shaded area. Black broken lines, singly differential cross sections calculated based on the formulas given by Cavaliere *et al.* [24].

given by

$$\frac{d^3\sigma_n}{d\Omega_a d\Omega_b dE_b} = J_n^2(\xi_{LA(e,2e)}) \frac{d^3\sigma_{FBA}}{d\Omega_a d\Omega_b dE_b}, \quad (10)$$

$$\xi_{LA(e,2e)} = \frac{\mathbf{E}_0}{\omega^2} \cdot (\mathbf{k}_i - \mathbf{k}_a - \mathbf{k}_b), \quad (11)$$

where \mathbf{k}_a is the electron wave vector for the fast electron and $\frac{d^3\sigma_{FBA}}{d\Omega_a d\Omega_b dE_b}$ is a field-free triply differential cross section calculated by first Born approximation, because, in the asymmetric configuration with the large (1000 eV) incident electron energy, the field-free triply differential cross section is described well by the first Born approximation [27]. In the numerical analysis below, we adopt the experimentally obtained triply differential cross section of the field-free ($e, 2e$) process as $\frac{d^3\sigma_{FBA}}{d\Omega_a d\Omega_b dE_b}$.

The n -photon LA($e, 2e$) intensity, $I_n(\theta_a, \phi_a, \theta_b, \phi_b, E_b)$, is proportional to $\rho_g(\mathbf{r})$, $\rho_e(\mathbf{r}, t)$, and the intensity of the ($e, 2e$) process under the field-free conditions, $I_0(\theta_a, \phi_a, \theta_b, \phi_b, E_b)$. In order to take account of the \mathbf{r} and t dependences of $\rho_g(\mathbf{r})$, $\rho_e(\mathbf{r}, t)$ and $\xi_{LA(e,2e)}(\mathbf{r}, t)$, we performed the spatiotemporal integration at given sets of the discrete values of θ_a , ϕ_a , θ_b , and E_b as

$$I_n(\theta_a, \phi_a, \theta_b, \phi_b, E_b) \propto \int_{x_{\min}}^{x_{\max}} dx \int_{y_{\min}}^{y_{\max}} dy \int_{z_{\min}}^{z_{\max}} dz \int_{t_{\min}}^{t_{\max}} dt$$

$$\times J_n^2 \left\{ \frac{\mathbf{E}_0(\mathbf{r}, t)}{\omega^2} \cdot [\mathbf{k}_i - \mathbf{k}_a(\theta_a, \phi_a, E_b) - \mathbf{k}_b(\theta_b, E_b)] \right\} \times \rho_g(\mathbf{r}) \rho_e(\mathbf{r}, t) I_0(\theta_a, \phi_a, \theta_b, \phi_b, E_b) \quad (12)$$

where $I_0(\theta_a, \phi_a, \theta_b, \phi_b, E_b)$ is the intensity of the ($e, 2e$) process under the field-free conditions. Note that ϕ_b is not a variable of the integration because $\mathbf{k}_b(\theta_b, \phi_b, E_b)$ has the axial symmetry around the z axis, which is parallel to the laser polarization direction.

In a similar manner as in the integrals in Eq. (6), the integrals in Eq. (12) are evaluated numerically at given sets of discrete numerical values of $(\theta_a, \phi_a, \theta_b, E_b)$. For the scattering angle θ_a , nine values in the range between 0° and 4° at an interval of 0.5° are adopted, and, for the azimuthal angle ϕ_a , 12 values in the range of 360° at an interval of 30° are adopted. For the scattering angle θ_b , five values in the range between 0° and 40° at an interval of 10° are adopted. For the energy of the slow electron, E_b , 11 values in the range between 0 and 10 eV at an interval of 1 eV are adopted. In a similar manner as in the evaluation of the LAES intensity, the effect of the inhomogeneity in the position dependence of the detector sensitivity and the existence of a thin shadow area where the scattered electrons are blocked by the gold wire ($\phi_a \sim 270^\circ$) are automatically compensated in the simulation. After evaluating the integrals of Eq. (12) for each $(\theta_a, \phi_a, \theta_b, E_b)$, $I_n(\theta_a, \phi_a, \theta_b, \phi_b, E_b)$ are calculated using the experimentally obtained $I_0(\theta_a, \phi_a, \theta_b, \phi_b, E_b)$ for the field-free case.

In Figs. 6(d) and 6(e), the results of the numerical simulations represented with the green solid lines with the filled area underneath are compared with the experimental LA(e , $2e$) spectra. It can be seen in Fig. 6(e) that the experimental intensity profile for $n = +1$ is in good agreement with the theoretical LA(e , $2e$) spectrum, but the intensity of the experimental LA(e , $2e$) spectrum is approximately twice as large as that of the theoretical spectrum.

In Figs. 7(a) and 7(b), the data connected by the red filled circles show the singly differential cross sections of the LA(e , $2e$) process for the fast scattered electrons as a function of the scattering angles and the azimuthal angles, respectively, calculated by the observed 2D map of the scattered electrons and the ejected electrons in the sum energy range of 985.3–986.0 eV, and the data connected by the black lines are the simulated cross sections. In Figs. 7(c) and 7(d), the data for the slow ejected electrons corresponding to those for the fast scattered electrons shown in Figs. 7(a) and 7(b) are shown. It can be seen in Figs. 7(a)–7(d) that the intensities of the experimental LA(e , $2e$) signals are mostly larger to a certain extent than those obtained by the theoretical calculations. As a result, the intensity of the experimental LA(e , $2e$) spectrum obtained after the integration of the signals over the detection angle ranges is approximately twice as large as that of the theoretical spectrum as shown in Fig. 6(e).

The larger intensity of the recorded LA(e , $2e$) signals than the theoretical estimate can be attributed to the interaction between an Ar atom and the laser field, which is neglected in the theoretical treatment of the LA(e , $2e$) processes above. In an intense laser field, Ar in the electronic ground state can be mixed with the electronically excited states the electronic configurations of which are $(3p)^5(ns)^1$ ($n > 3$) and $(3p)^5(nd)^1$ ($n \geq 3$) through the formation of the dressed states. As has been theoretically shown by Joachain *et al.* [16] and Martin *et al.* [17] for the LA(e , $2e$) process of a hydrogen atom and by Khalil *et al.* [28] for a helium atom in an intense laser field, the enhancement of the triply differential cross section of the LA(e , $2e$) process of Ar can also be ascribed to the formation of the light-dressed states. Once the light-dressed states are formed, the LA(e , $2e$) process can be regarded as the electron-impact ionization via a light-dressed state. Because

the cross sections of the electron-impact ionization of the electronically excited states of Ar are one to two orders of magnitude larger than that of the ground state [25,29], it is expected that the LA(e , $2e$) process enhances the triply differential cross sections. So far, theoretical studies of a LA(e , $2e$) process in which a light-atom interaction is taken into account have been reported only on one-electron and two-electron systems [11]. Development of theoretical frameworks is highly awaited [30,31] so that we will be able to extract how and to what extent atomic and molecular orbitals are deformed by an external laser field based on experimental data of an enhancement of the triply differential cross sections of the LA(e , $2e$) process.

IV. SUMMARY

We designed and constructed an apparatus equipped with two ARTOF analyzers placed in the asymmetric configuration to measure (e , $2e$) processes in ultrashort intense laser fields. Using the apparatus, we have observed the one-photon energy gain in the LA(e , $2e$) process in the ultrashort-pulsed intense laser field. We showed that the signal intensity of the LA(e , $2e$) $n = +1$ process obtained by integrating the signals over the detection angle ranges is about twice as large as that estimated by the theoretical calculations in which the interaction between a target atom (Ar) and the light field is neglected. We ascribed this discrepancy to the formation of the light-dressed states of Ar. The measurement of a triply differential cross section of the LA(e , $2e$) process will provide us with valuable data by which we can discuss how the formation of the light-dressed states deforms orbitals of multielectron atomic and molecular systems interacting with the light field.

ACKNOWLEDGMENT

This work was supported by Japan Society for the Promotion of Science KAKENHI Grants No. JP24245003, No. JP15H05696, No. JP17H03004, No. JP17K14431, and No. JP19K15498.

-
- [1] H. Ehrhardt, K. Jung, G. Knoth, and P. Schlemmer, *Z. Phys. D* **1**, 3 (1986).
 - [2] H. Ehrhardt, K. H. Hesselbacher, K. Jung, E. Schubert, and K. Willmann, *J. Phys. B* **7**, 69 (1974).
 - [3] M. Takahashi, *Bull. Chem. Soc. Jpn.* **82**, 751 (2009).
 - [4] B. Wallbank, V. W. Connors, J. K. Holmes, and A. Weingartshofer, *J. Phys. B* **20**, L833 (1987).
 - [5] W. R. Newell, in *Thirteenth International conference on atomic physics (ICAP-13)*, edited by H. Walther, T. W. Hensch, and B. Neizert, AIP Conf. Proc. No. 275 (AIP, New York, 1993), p. 540.
 - [6] N. J. Mason, *Rep. Prog. Phys.* **56**, 1275 (1993).
 - [7] F. Ehlötzky, A. Jaroń, and J. Z. Kamiński, *Phys. Rep.* **297**, 63 (1998).
 - [8] Y. Morimoto, R. Kanya, and K. Yamanouchi, *Phys. Rev. Lett.* **115**, 123201 (2015).
 - [9] K. Ishida, Y. Morimoto, R. Kanya, and K. Yamanouchi, *Phys. Rev. A* **95**, 023414 (2017).
 - [10] R. Kanya and K. Yamanouchi, *Atoms* **7**, 85 (2019).
 - [11] A. Makhoute, D. Khalil, and I. Ajana, *Atoms* **7**, 40 (2019).
 - [12] M. Mohan and P. Chand, *Phys. Lett. A* **65**, 399 (1978).
 - [13] Y. Morimoto, R. Kanya, and K. Yamanouchi, *J. Chem. Phys.* **140**, 064201 (2014).
 - [14] C. Höhr, A. Dorn, B. Najjari, D. Fischer, C. D. Schröter, and J. Ullrich, *Phys. Rev. Lett.* **94**, 153201 (2005).
 - [15] C. Höhr, A. Dorn, B. Najjari, D. Fischer, C. D. Schröter, and J. Ullrich, *J. Electron. Spectrosc. Relat. Phenom.* **161**, 172 (2007).

- [16] C. J. Joachain, P. Francken, A. Maquet, P. Martin, and V. Veniard, *Phys. Rev. Lett.* **61**, 165 (1988).
- [17] P. Martin, V. Veniard, A. Maquet, P. Francken, and C. J. Joachain, *Phys. Rev. A* **39**, 6178 (1989).
- [18] R. Kanya, Y. Morimoto, and K. Yamanouchi, *Phys. Rev. Lett.* **105**, 123202 (2010).
- [19] R. Kanya, Y. Morimoto, and K. Yamanouchi, *Rev. Sci. Instrum.* **82**, 123105 (2011).
- [20] T. Y. Suzuki, H. Suzuki, S. Ohtani, T. Takayanagi, and K. Okada, *Phys. Rev. A* **75**, 032705 (2007).
- [21] W. F. Chan, G. Cooper, X. Guo, G. R. Burton, and C. E. Brion, *Phys. Rev. A* **46**, 149 (1992).
- [22] N. M. Kroll and K. M. Watson, *Phys. Rev. A* **8**, 804 (1973).
- [23] N. L. S. Martin, C. M. Weaver, B. N. Kim, and B. A. deHarak, *Phys. Rev. A* **99**, 032708 (2019).
- [24] P. Cavaliere, G. Ferrante, and C. Leone, *J. Phys. B* **13**, 4495 (1980).
- [25] L. K. Jha, S. Kumar, and B. N. Roy, *Eur. Phys. J. D* **40**, 101 (2006).
- [26] M. Jain and N. Tzoar, *Phys. Rev. A* **18**, 538 (1978).
- [27] F. W. Byron and C. J. Joachain, *Phys. Rep.* **179**, 211 (1989).
- [28] D. Khalil, A. Maquet, R. Taïeb, C. J. Joachain, and A. Makhoute, *Phys. Rev. A* **56**, 4918 (1997).
- [29] H. Deutsch, K. Becker, A. N. Grum-Grzhimailo, K. Bartschat, H. Summers, M. Probst, S. Matt-Leubner, and T. D. Märk, *Int. J. Mass Spectrom.* **233**, 39 (2004).
- [30] A. S. Zaytsev, S. A. Zaytsev, L. U. Ancarani, and K. A. Kouzakov, *Phys. Rev. A* **97**, 043417 (2018).
- [31] S. A. Zaytsev, A. S. Zaytsev, L. U. Ancarani, and K. A. Kouzakov, *Eur. Phys. J. D* **73**, 42 (2019).